Geophysical Research Letters

RESEARCH LETTER
10.1029/2018GL080667

Key Points:
- A fire-generated vortex produced tornado-strength winds, extreme fire behavior, and devastated parts of Redding, California
- The vortex exhibited tornado-like dynamics, emerging from a shear zone during the rapid development of a pyrocumulonimbus

Supporting Information:
- Supporting Information S1
- Movie S1
- Movie S2

Correspondence to:
N. P. Lareau,
nlareau@unr.edu

Citation:
Lareau, N. P., Nauslar, N. J., & Abatzoglou, J. T. (2018). The Carr fire vortex: A case of pyrotornadogenesis? *Geophysical Research Letters, 45*, 13,107–13,115. https://doi.org/10.1029/2018GL080667

Received 27 SEP 2018
Accepted 18 NOV 2018
Accepted article online 21 NOV 2018
Published online 3 DEC 2018
Corrected 15 APR 2019

This article was corrected on 15 APR 2019. See the end of the full text for details.

The Carr Fire Vortex: A Case of Pyrotornadogenesis?

N. P. Lareau[1], N. J. Nauslar[2], and J. T. Abatzoglou[3]

[1]Department of Physics, University of Nevada, Reno, Reno, NV, USA, [2]Storm Prediction Center, NCEP, NWS, NOAA, Norman, OK, USA, [3]Department of Geography, University of Idaho, Moscow, ID, USA

Abstract Radar and satellite observations document the evolution of a destructive fire-generated vortex during the Carr fire on 26 July 2018 near Redding, California. The National Weather Service estimated that surface wind speeds in the vortex were in excess of 64 m/s, equivalent to an EF-3 tornado. Radar data show that the vortex formed within an antecedent region of cyclonic wind shear along the fire perimeter and immediately following rapid vertical development of the convective plume, which grew from 6 to 12 km aloft in just 15 min. The rapid plume development was linked to the release of moist instability in a pyrocumulonimbus (pyroCb). As the cloud grew, the vortex intensified and ascended, eventually reaching an altitude of 5,200 m. The role of the pyroCb in concentrating near-surface vorticity distinguishes this event from other fire-generated vortices and suggests dynamical similarities to nonmesocyclonic tornadoes.

Plain Language Summary A tornado-strength fire-generated vortex devastated portions of Redding, California, during the Carr fire on 26 July 2018. In this study, satellite and radar observations document the evolution of the vortex, revealing similarities to tornado dynamics. A key factor in the vortex formation was the development of a fire-generated ice-topped cloud (i.e., a pyrocumulonimbus), which reached as high as 12 km aloft. The development of the cloud helped stretch the underlying column of air, thereby concentrating the rotation near the surface and causing the tornado strength winds, estimated at ~64 m/s. These observations will help forecasters and scientists identify, and potentially warn for, future destructive fire-generated vortices.

1. Introduction

Destructive fire-generated vortices (FGVs) can occur in both urban and wildland fires (Forthofer & Goodrick, 2011). These vortices feature upright columns of vigorously rotating ash, smoke, and often flame (Tohidi et al., 2018). Whereas most FGVs are small (<10-m diameter), some large vortices (>100-m diameter) can generate tornado strength winds, and in very rare cases, actual tornadoes can form when a FGV is linked to an overlying pyrocumulonimbus (hereafter pyroCb; Fromm et al., 2010). For example, the Canberra Firestorm of 2003 produced the sole documented case of pyrotornadogenesis, forming a long-track (20 km) F2-intensity tornado connected to a deep pyroCb (Cunningham & Reeder, 2009; Fromm et al., 2006; hereafter CR09; McRae et al., 2013).

Pyrotornadoes are dynamically distinct from other FGVs in that the concentration and stretching of near-surface vorticity are accomplished by both the fire-induced updrafts and the pyroCb latent heat release. Specifically, the latent heating reinvigorates the updraft aloft (Freitas et al., 2007; Luderer et al., 2006, 2009; Trentmann et al., 2006) and thereby enhances vortex stretching in the underlying column (CR09). In contrast, nontornadic FGVs concentrate vorticity solely by fire processes (Forthofer & Goodrick, 2011, Tohidi et al., 2018; hereafter T18). In both tornadic and nontornadic FGVs, the initial source of near-surface rotation can include tilting of boundary layer wind shear (Church et al., 1980), differential heating by the fire (CR09; T18), spatial variations fire processes (Kuwana et al., 2013; Zhou & Wu, 2007), mesoscale to synoptic processes (Seto & Clements, 2011; Umscheid et al., 2006), and flow-topography interactions (Countryman, 1971; Sharples et al., 2015).

While numerical simulations (CR09) and laboratory studies (summarized in T18) can help establish and test mechanisms for FGV development, there remains a need to confront these idealizations with observations. Unfortunately, observations of large FGVs, including pyrotornadoes, are only available in a handful of cases (Church et al., 1980; Banta et al., 1992; Clements et al., 2018; Fromm et al., 2006; McCarthy et al., 2017; McRae et al., 2013) and yield limited insights into the origins of rotation and the role of pyroCbs in vortex stretching. In this study, we leverage high-resolution radar, satellite, and model analyses to document the

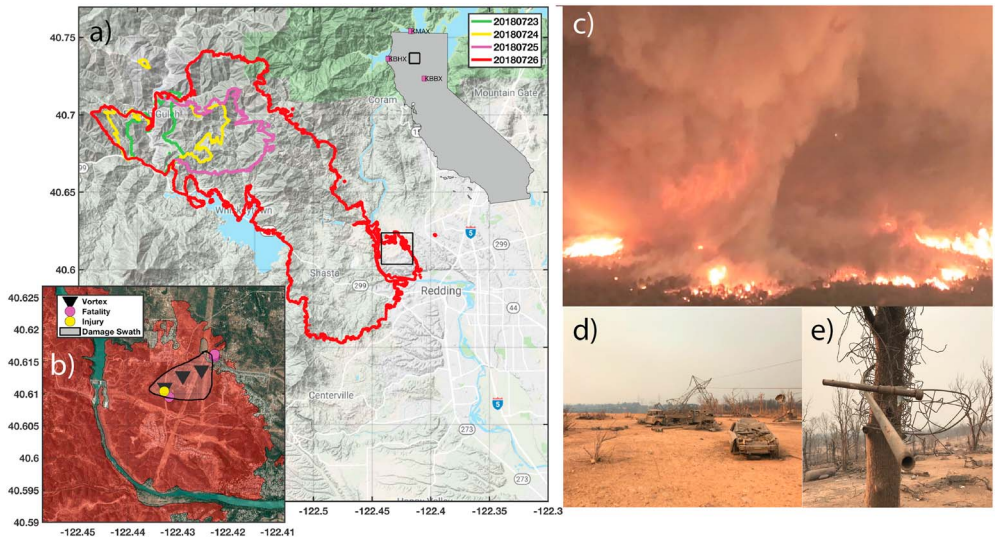

Figure 1. Overview of the fire vortex that formed during the Carr fire on 26 July 2018. (a) Map showing the terrain and fire progression from 23 to 27 July 2018. (b) Detailed map of the vortex progression, approximate damage swath, and the locations of injuries and fatalities. (c) Video still showing the structure of the vortex. Video courtesy of CalFire. (d and e) Photographic evidence of damage, courtesy of (c) CalFire, (b) Damon Arthur, and (c) Craig Clements.

evolution of a tornado-strength FGV that devastated portions of Redding, California, during the Carr fire on 26 July 2018 (Figure 1). These data are used to establish antecedent vorticity sources, the impact of pyroCb processes on the vortex formation, and to ask the question, "is this a case of pyro-tornadogenesis?"

2. Data and Methods

2.1. Radar Data

National Weather Service Next Generation Weather Radar (NEXRAD) radars located at Beal Air Force Base, CA (KBBX); Eureka, CA (KBHX); and Medford, OR (KMAX) are used to observe the wildfire plume and vortex evolution (radar locations in Figure 1a). Centimeter wavelength radars, including NEXRAD, are sensitive to ash lofted in the plume and have thus been used in numerous wildfire studies (e.g., Banta et al., 1992; Jones & Christopher, 2010; McCarthy et al., 2017). All three radars are used to examine the plume structure, whereas only KBBX (142 km away) is used to identify *radar vortex signatures*, which are compact regions of azimuthally adjacent in and outbound flows (Brown et al., 1978). Specifically, data from the first four elevations, intersecting the plume at 2.5, 3.49, 4.54, and 5.69 km mean sea level (MSL), are used compute the 0.5° gate-to-gate difference in the radial wind component. The radar completes one sweep in ~15 s and full volumes every 3 min.

2.2. Satellite Data

GOES-16 data are also used to characterize the plume and fire evolution. Specifically, the visible band (0.64 μm) is used to examine pyroCb growth, near-infrared bands (1.6, 2.2, and 3.9 μm) are used to examine the *Fire Temperature*, and the 11-μm band is used to characterize cloud top temperature. An overview of GOES-16 bands, including their spatial resolution, is available at https://www.goes-r.gov/education/ABI-bands-quick-info.html. GOES-15 data are also used in a supplemental analysis (Figure S2).

2.3. Ancillary Data

High Resolution Rapid Refresh (HRRR) and Rapid Refresh (RAP) model analysis fields are used to characterize surface winds, relative vorticity, and thermodynamics near the fire. The North American Regional Reanalysis (NARR), surface weather observations (via MesoWest; Horel et al., 2002), and gridded surface meteorological data from Abatzoglou (2013) provide historical context for weather and climate conditions leading up to the fire. The fire progression is determined using fire perimeters from the National Infrared Operations (NIROPS; http://nirops.fs.fed.us/).

3. Results

3.1. Carr Fire Progression

The Carr fire started from a vehicle malfunction on 23 July 2018 and went on to burn 92,936 ha, making it the seventh largest fire in California (CA) history at the time of this writing. The fire resulted in six fatalities and destroyed 1,079 residences (CalFire, 2018). Following ignition, the fire was initially *terrain driven*, spreading uphill on 23–25 July (Figure 1a). In contrast, on 26 July the fire became *wind driven*, advancing rapidly eastward and downhill into western suburbs of Redding. The fire jumped the Sacramento River, and between 0220 and 0300 UTC on 27 July a large FGV formed along the northeastern flank of the fire (Figure 1b). The National Weather Service estimated that the vortex winds exceeded 64 m/s, equivalent to an EF-3 tornado. Figure 1c shows a video snapshot of the FGV indicating vigorous rotation, large flame lengths, and lofted burning debris (see Movies S1 and S2). The vortex damage swath (Figure 1b) was ~1 km long and included downed electrical towers (Figure 1d), a steel pipe wrapped around power poles (Figure 1e), and other extensive damage. The FGV was directly related to four deaths (locations in Figure 1b), numerous injuries, and substantive loss of property (CalFire).

3.2. Climate and Fuels

Several climatic factors enabled heighted fire activity across northern CA during the summer of 2018. After a protracted drought from 2012 to 2016, the region saw near record precipitation (~50% above normal) during the wet season of October 2016 to May 2017. Increased precipitation can increase fine fuel loading (i.e., grasses) that subsequently increases fire potential once cured, often in the following year (Abatzoglou & Kolden, 2013). By contrast, the wet season from October 2017 to May 2018 had very low precipitation across the region (50% below normal) allowing fuels to reach critical flammability earlier in the year than normal. Compounding the effects of dry antecedent conditions, July 2018 was the warmest month on record in Redding (KRDD, 1972–2018) and for the Sacramento Drainage climate division (1895–2018). The anomalous heat was marked by monthly low temperatures >3 °C above 1981–2010 means in mountain and foothill locations, including where the Carr fire burned. The nighttime warmth likely inhibited typical *nocturnal recovery* of relative humidity, thereby contributing to the critically dry fuels (100-hr dead fuel moisture) on the date of the vortex (Figure 2a). Collectively, these factors set the stage for the Carr fire and other large fires in the region, including the Ranch Fire, which became the largest fire in CA modern history.

3.3. Fire Weather Conditions

While climatic factors set stage, synoptic and mesoscale weather contributed to the rapid fire progression and vortex generation on 26 July. The day was marked by daily record high temperature at KRDD (45 °C) and exceptionally low relative humidity ($<3.5\%$). The heat was linked to an upper level ridge (not shown) and a deep West Coast Thermal Trough (Brewer et al., 2012) with an embedded thermal low over the northern Sacramento River valley (Figures 2b and 2c). The daytime deepening of the thermal low acted in conjunction with cold marine air along the CA coast to generate a strong SE-NW oriented pressure gradient (90th percentile for July between KBHX to KRDD). The anomalous pressure gradient generated a late afternoon northwesterly wind across the Klamath mountains that spilled into the Sacramento Valley (Figures 2b and 2c). This northwest wind was the main driver for the rapid eastward and downslope advance of the fire toward Redding, as shown in Figure 1a.

The northwesterly flow also introduced two vorticity sources that likely contributed to the vortex generation. First, the boundary between the northwesterly and southerly flows provided a strip of cyclonic relative vorticity oriented from southwest to northeast at 02 UTC, according to HRRR analyses (Figure 2b). Second, wind shear and flow curvature due to terrain-flow interaction near Whiskeytown Lake (see Figure 1a) formed a localized region of enhanced cyclonic vorticity over the northern fire perimeter even as the wind shift boundary progressed eastward (Figure 2c). Combined, these processes produced a persistent local maximum in cyclonic relative vorticity proximal to the location of vortex formation. Notably, HRRR analyses on adjacent days show similar cyclonic shear zones, suggesting that these are robust features of the flow-topography interaction and diurnal winds.

The HRRR, however, does not simulate flow modifications due to the fire and thus incompletely represent the winds at the time of vortex generation. For example, strong localized gradients in buoyancy spanning the fire line likely generate horizontal axis vorticity near the surface, which may later be tilted into the vertical and

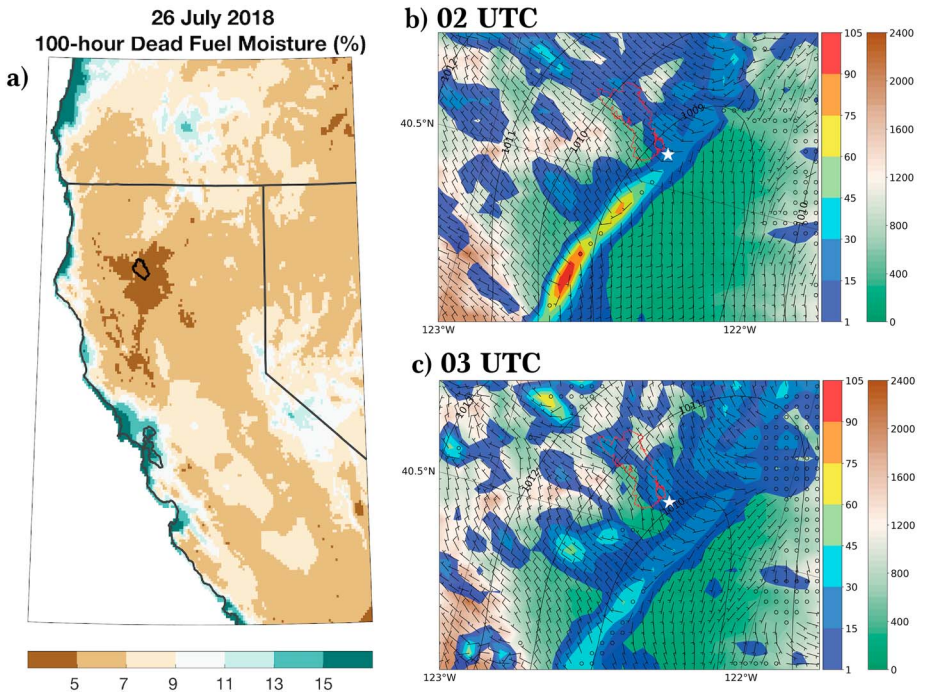

Figure 2. Summary of fuels and weather characteristics contributing to the Carr Fire. (a) The 100-hr dead fuel moisture percent. Data from Abatzoglou (2013). The perimeter of the Carr fire is shown in black for reference. (b and c) High Resolution Rapid Refresh surface analysis for 02 and 03 UTC on 27 July 2018 showing mean sea level pressure (black contours), wind barbs, terrain (shaded, green to brown in meters), cyclonic relative vorticity (shaded, in increments of 10^{-4}/s), and the Carr fire perimeter (red). Redding, CA, is indicated with a white star.

ingested into an updraft to form a coherent vortex (T18). The concavity of the fire flank may also aid in vortex generation, suggesting qualitative similarities to the distribution of diabatically generated outflow boundaries and horizontal axis vorticity found in many tornadic supercellular storms (Doswell & Burgess, 1993).

3.4. Vortex Evolution

The Carr fire vortex was observed at high spatial and temporal resolution by the KBBX radar (Figure 3). In this portion of the analysis, the velocity data are averaged over four successive radar sweeps (~12 min) at each elevation to succinctly summarize the vortex evolution (Figures 4a–4p). In the hour prior to the vortex formation (Figures 3a–3d), radar data show a broad region of cyclonic shear between the northwesterly flow over the fire (blue shading) and southeasterly flow (orange and red shading) to the northeast of the fire perimeter. The shear is concentrated along the fire flank, consistent with the HRRR analysis but also suggesting the role of fire-modified winds. The strength of the shear increases from 0144 to 0220 UTC, but no radar vortex signature is apparent during that time.

A distinct vortex signature emerges between 0224 and 0236 UTC (Figure 3e), consistent with timing established in video evidence (CalFire). The vortex subsequently intensifies until 0248 UTC, exhibiting an increase in radial velocity, but very little horizontal displacement (Figure 3f). The vortex is approximately centered on the fire perimeter and remains embedded within the broader cyclonic shear zone throughout its evolution.

The vortex becomes increasingly vertically coherent with time as the vortex signature appears in tilt 2 by 0236 UTC (3.49 km MSL; Figure 3h) and tilt 3 by 0248 UTC (4.54 km MSL; Figure 3l). Interestingly, the vortex signature is absent farther aloft (tilt 4, 5.69 km) where radial divergence is instead observed (Figures 3n–3p). These observations show the following: (1) The vortex grows from the bottom up, reaching a maximum vertical extent of ~5,200 m (i.e., between tilts 3 and 4), and (2) the vortex is linked to divergence in the overlying pyroCb plume, forming an *in, up, and out* circulation. The bottom-up evolution, antecedent source of wind shear, and the link to a developing convective plume (discussed below) are all consistent with the

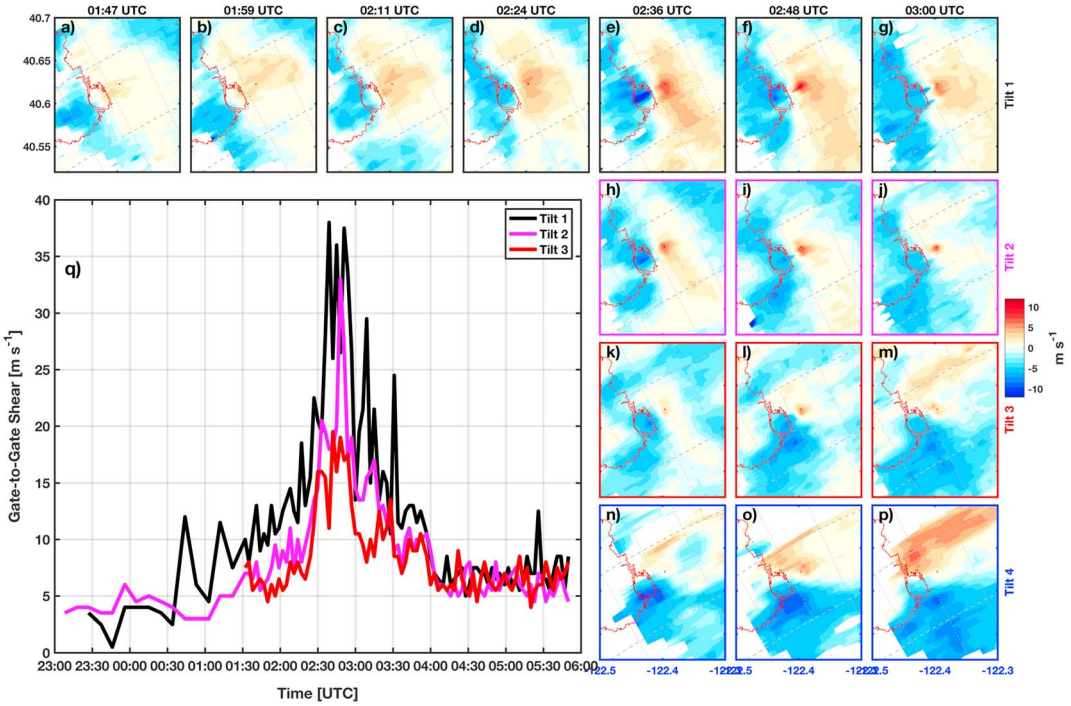

Figure 3. Radar summary of the vortex evolution. Individual panels (a–p) show 12-min average radial velocity for tilt 1 (a–g), tilt 2 (h–j), tilt3 (k–m), and tilt 4 (n–p). The fire perimeter is shown in red for local midnight on 26 July 2018. The data for tilts 2–4 are only shown after 0236 UTC to emphasize the period of a vertically coherent vortex. (q) The time series of maximum gate-to-gate wind difference for each of the three lowest tilts. The line colors correspond to axis colors for the individual panels.

mechanisms for nonmesocyclonic tornadogenesis (Lee & Wilhelmson, 1997; Trapp et al., 1999; Wakimoto & Wilson, 1989).

Since the data in Figures 3a–3p are space and time averaged they mask the peak magnitude of the wind shear associated with the vortex. To better characterize these winds, Figure 3q presents the time series of

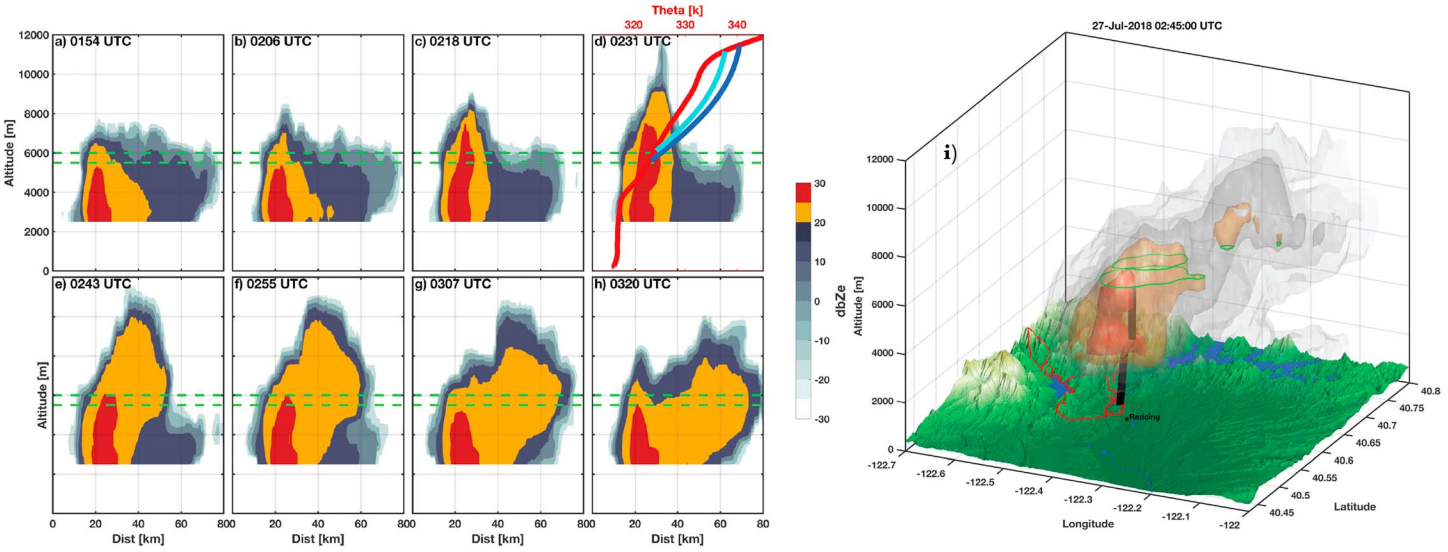

Figure 4. Overview of plume and pyroCb development. (a–h) Radar reflectivity cross sections showing the plume growth (a–d) and decay (e–h). In (d) the RAP 0200 UTC potential temperature profile (red line) and the estimated pyroCb potential temperature profiles (blue, cyan) are shown, corresponding to the top axis. The green dashed line shows the estimated cloud base heights of 5,500 and 6,000 m. (i) 3-D rendering of radar reflectivity isosurfaces at 29 (red), 24 (orange), 20–10 (gray shades) dbZe. The vortex center locations are shown as the solid black line. The cloud base heights are shown as green contours.

maximum gate-to-gate wind differences (hereafter *shear*) for the lowest three elevation angles. The shear is strongest at the lowest tilt (black line, Figure 3q), increasing gradually from 0130 to 0215 UTC then rapidly up until 0248 UTC, reaching a peak of ~37 m/s. The timing of the intensification is similar across all tilts, with peak shears of 33 and 19 m/s at tilts 2 and 3, respectively. After 0248 UTC the vortex diminishes at all levels and by 0330 UTC only a broad mesocyclonic rotation persists (not shown).

To contextualize these observations, the vortex strength can also be expressed as a rotational wind (half the shear) and thereby compared with NEXRAD observations from a large sample of ordinary tornadic storms compiled in Smith et al. (2015). The maximum FGV rotational winds (18.5 m/s) fall in the interquartile range of EF1–2 tornadoes linked to quasi-linear convective systems and EF0–1 tornadoes spawned from supercells (see Figure 7 in Smith et al., 2015). The estimated EF-3 surface winds in the Carr fire vortex exceed these intensity classifications, which may reflect contributions of fire processes to vortex intensification, uncertainties in the wind estimates due to fire damage, or other unknown factors.

3.5. Links to the Pyrocumulonimbus

The intensification of the vortex from 0215 to 0248 UTC coincides with the rapid vertical development of the plume. Figures 4a–4d show a time sequence of radar reflectivity cross sections indicating a core of ash lofted in the updraft (>25 dbZ) as the plume top ascends from 6 to 12 km. This growth implies substantive stretching of the underlying column and a likely mechanism for the contemporaneous vortex intensification. After 0250 UTC the plume top subsides and reflectivity values diminish, indicative of column compression and decreased updrafts during the period of vortex decay (Figures 4e–4h).

The location of the vortex, at peak intensity, relative to the broader convective plume is further examined in Figure 4i, which presents reflectivity isosurfaces and the center locations of the vortex (black line). At 0245 UTC the vortex is located east of the core of highest reflectivity in the updraft and remains vertical to ~5,200 m, where the plume becomes sheared by the southwesterly flow aloft.

While fire generated buoyancy drives the initial plume development, we hypothesize that the rapid growth from 0215 to 0248 occurs due to the release of moist instability aloft. To test this hypothesis, we examine the thermodynamics of cloud parcels (blue and cyan lines, Figure 4d) in relation to the RAP potential temperature profile over Redding, CA, at 02 UTC (red line, Figure 4d). The cloud base heights are estimated to fall between 5,500 and 6,000 m based on spatial gradients in the radar echo tops during the onset of moist convection (Figure S2). This range of cloud bases is consistent with the RAP-derived convective condensation level of 5,944 m. Lareau and Clements (2016) show that the convective condensation level is a good proxy for pyroCb cloud base despite many uncertainties in the thermodynamics of fire-modified parcels (e.g., Luderer et al., 2009; Potter, 2005; Tory et al., 2018).

Based on these cloud base height estimates, we examine moist-adiabatic ascents starting at both 5,500 and 6,000 m to represent in cloud profiles (cyan and blue lines, Figure 4d). These cloudy parcels produce 753 and 418 J/kg of convective available potential energy and reach neutral buoyancy at 11260 and 11561 m, respectively (see also Figure S3). This is in good agreement with the radar-derived cloud top heights, which reach a mean (maximum) of 11,472 (11,887) m between 0230 and 0300 UTC (Figure S1). While these thermodynamic estimates neglect some processes, including entrainment into the pyroCb, they highlight two factors that inform our interpretation of the event:

There is sufficient moist instability for fire-heated parcels to trigger a deep convective cloud, thereby contributing to the rapid plume growth from 6 to 12 km during the vortex intensification.

The estimated vortex top (~5,200 m) is close to cloud base but may not directly connect to the cloud. Some authors suggest that the connection of a vortex to cloud base is a necessary condition for a tornado, whereas others allow for vortices to be classified as tornadic provided they are dynamically linked to cloud processes (see discussion in Agee & Jones, 2009).

The role of moist instability in the plume growth is further evidenced in GOES-16 visible imagery, which shows the rapid pyroCb development (Figures 5a–5c). The cloud first appears as a *bright white* protrusion that casts a long shadow across the otherwise capped smoke layer (Figure 5b; see also Figure S2). As the cloud growth continues (Figure 5c) it exhibits the same sheared structure apparent in the radar observations (e.g., Figure 4i). After this time a glaciated anvil detrains from the plume and advects to the northeast

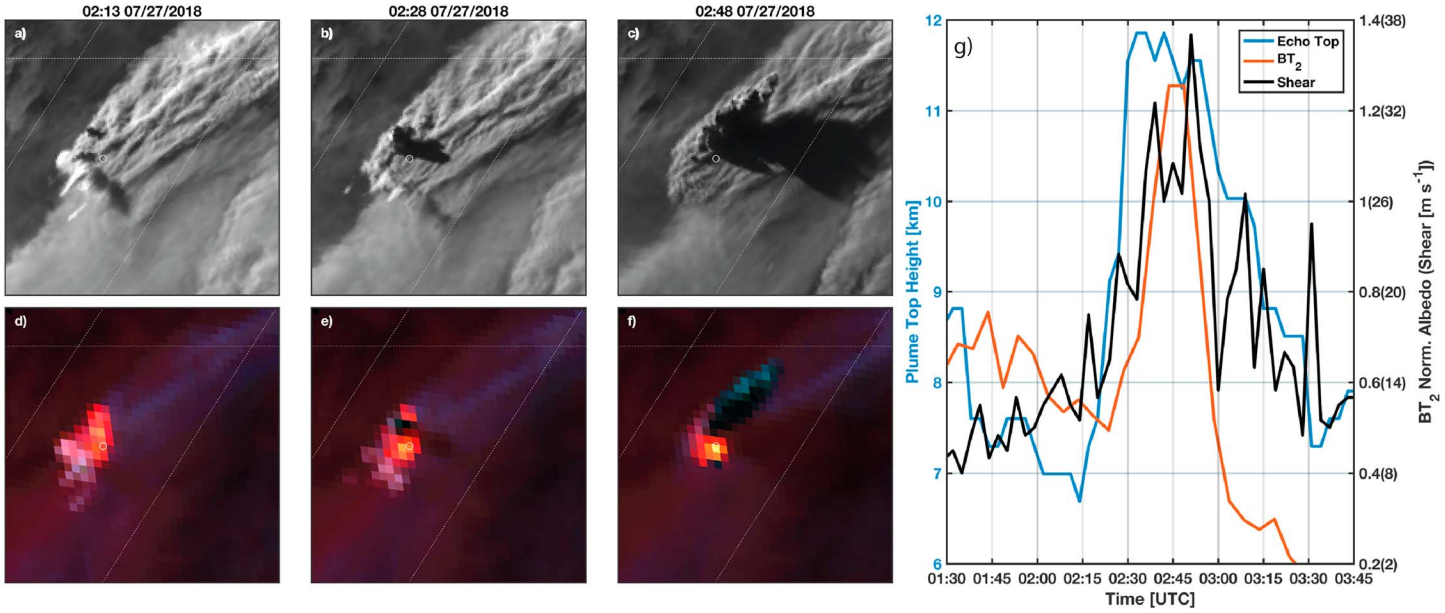

Figure 5. Overview of GOES-16 observations of the pyroCb and fire evolution. (a–c) GOES-16 visible (0.64 μm) observations of the pyroCb growth. (d–f) GOES-16 *Fire Temperature RGB* product showing the fire progression and intensification (warm colors) and cloud top cooling (cool colors). (g) Comparative time series of the plume height (blue line), vortex strength (black line), and 2.2-μm normalized albedo, which is a measure of fire intensity.

while the convective column dissipates (as shown in Figures 5e–5h). The classification of the cloud as a pyroCb is determined from both the 11-μm cloud top temperature (not shown), which drops below 235 K (Peterson, Fromm, et al., 2017; Peterson, Hyer, et al., 2017), and the RAP-sounding temperature corresponding to the radar echo tops, which is as cold as 223 K.

3.6. Links to Fire Behavior

GOES-16 infrared data establish temporal and spatial links among the pyroCb, vortex, and fire behavior. Figures 5d–5f show the *fire temperature* imagery, revealing the eastward expansion and overall intensification of the fire during the pyroCb development and vortex intensification. Notably, the fire temperature peaks in the pixel corresponding to the vortex location, indicative of the intense combustion associated with rotating column. Also apparent in these data are the cooling of the pyroCb cloud tops (blue shades) with time.

The temporal coevolution of the plume height, fire intensity, and vortex strength are further examined in Figure 5g. The fire temperature increase is apparent in the 2.2-μm *albedo*, which is sensitive to temperatures hotter than 600 K and thus represents regions of intense combustion (i.e., hotter fires radiate at shorter wavelengths). The value is expressed as an albedo, rather than brightness temperature, because it is normalized by the top-of-atmosphere solar radiation at this wavelength. The intense combustion was likely related to both the vortex dynamics (i.e., reduced entrainment and enhanced inflow; T18) and the urban fuels consumed (e.g., houses). Interestingly, the increase in fire temperature lags the plume development but is mostly in phase with the vortex intensification (Figure 5g). This temporal lag further suggests the leading role of the pyroCb initiation in vortex intensification and thus the extreme fire behavior.

4. Conclusions

The radar, satellite, and other observations during the Carr fire paint a clear picture of the sequence of events leading to the vortex development and intensification:

1. Anomalously low fuel moisture, record heat, and other factors set the stage for fast moving fires.
2. A near-surface cyclonic shear zone developed in the hour prior to vortex formation. This shear zone is readily apparent in the radar data and likely linked to a topographic eddy and fire-modified winds.
3. The tornado-strength vortex subsequently formed within the preexisting shear zone immediately following the rapid vertical development of a pyroCb, fueled by the release of moist instability aloft.

4. The vortex intensified and ascended with time, extending close to the pyroCb cloud base. This evolution suggests a link between the dynamics aloft and those at the surface.
5. The vortex dissipated as the pyroCb anvil detrained and the plume core subsided.

This sequence suggests that the Carr fire vortex may qualify as pyrogenetic tornado and not merely a tornado-strength FGV. Specifically, the latent heating within the pyroCb and subsequent vertical stretching of antecedent near-surface vorticity are key ingredients to the vortex formation. These factors differentiate this vortex from ordinary FGVs and are consistent with theories for nonmesocyclonic tornadogenesis in environments with high cloud bases and steep lapse rates (Agee & Jones, 2009; Davies, 2006; Wakimoto & Wilson, 1989).

However, the Carr fire vortex also differs from both ordinary tornadoes and the only other documented pyrotornado during the Canberra Firestorm. First, despite the importance of pyroCb processes, the vortex was not definitely pendant from the cloud base, a necessary condition for a tornado according to some, but not all, researchers. Second, whereas the Canberra pyrotornado produced a 20-km damage track and repeatedly lifted from the surface, the Carr fire vortex remained fixed to the fire perimeter for ~30 min, traveling only ~1 km. This persistent link to the fire suggests that fire processes remained important in concentrating the surface vorticity, even during the pyroCb growth. In light of these complexities, future modeling studies will be required to fully elucidate the origins rotation, the role of fire heat and moisture fluxes, contributions to vorticity due to fire line geometry, and the impact of the pyroCb on the vortex evolution. Results from these simulations may contribute to our ability to classify this FGV as tornadic or not.

Irrespective of the nomenclature, the societal impact of this event warrants discussion of the potential to warn for future tornado-strength FGVs and other manifestations of extreme fire behavior. In this case, the availability of high-resolution radar and satellite data provides advance indications for vortex formation. The operational meteorological and fire-fighting communities might develop routines to carefully inspect these sorts of data for evidence of plume rotation and rapid fire advance toward populations centers, thereby informing early warnings and evacuation decisions. Forecast offices might also identify diurnal and terrain-driven flows that may locally enhance the risk of FGVs during a given fire. While tornado-strength FGVs will remain rare events, the recent uptick in wildfire impacts on population centers (e.g., Nauslar et al., 2018) underscores the need for continued research into all forms of extreme fire behavior.

Acknowledgments
Funding for this work is provided, in part, by the National Science Foundation under grant AGS-1807774. Additional funding is from the University of Nevada, Reno. We thank two anonymous reviewers for their comments, which improved this manuscript. We acknowledge and thank Mathew Roberts for initial recognition of the radar vortex signature in this event, Rob Elvington for local knowledge and documentation of the Carr fire, Damon Arthur and Craig Clements for photographs and descriptions of the damage, and Scott Murphy for video documentation of the onset of the vortex. We also thank the California Department of Forestry (CalFire) for videos that are included as supplemental material. All data used in this analysis are free and publicly available. NEXRAD and GOES-16 data can be obtained from the Amazon cloud at https://registry.opendata.aws/noaa-nexrad/ and https://registry.opendata.aws/noaa-goes/. HRRR data can be accessed via the University of Utah archive (doi: 10.7278/S5JQ0Z5B) courtesy of Brian Blaylock. NCEP Reanalysis data provided by the NOAA/OAR/ESRL PSD, Boulder, Colorado, USA, from their Web site at https://www.esrl.noaa.gov/psd/. RAP data are available at: https://nomads.ncdc.noaa.gov/data/rucanl/. Neil Lareau provides consulting services pertaining to wildfire plumes but is not retained for analysis of the Carr fire.

References

Abatzoglou, J. T. (2013). Development of gridded surface meteorological data for ecological applications and modelling. *International Journal of Climatology*, *33*(1), 121–131. https://doi.org/10.1002/joc.3413

Abatzoglou, J. T., & Kolden, C. A. (2013). Relationships between climate and macroscale area burned in the western United States. *International Journal of Wildland Fire*, *22*(7), 1003–1020. https://doi.org/10.1071/WF13019

Agee, E., & Jones, E. (2009). Proposed conceptual taxonomy for proper identification and classification of tornado events. *Weather and Forecasting*, *24*(2), 609–617. https://doi.org/10.1175/2008WAF2222163.1

Banta, R. M., Olivier, L. D., Holloway, E. T., Kropfli, R. A., Bartram, B. W., Cupp, R. E., & Post, M. J. (1992). Smoke-column observations from two forest fires using Doppler lidar and Doppler radar. *Journal of Applied Meteorology*, *31*(11), 1328–1349. https://doi.org/10.1175/1520-0450(1992)031<1328:SCOFTF>2.0.CO;2

Brewer, M. C., Mass, C. F., & Potter, B. E. (2012). The West Coast thermal trough: Climatology and synoptic evolution. *Monthly Weather Review*, *140*(12), 3820–3843. https://doi.org/10.1175/MWR-D-12-00078.1

Brown, R. A., Lemon, L. R., & Burgess, D. W. (1978). Tornado detection by pulsed Doppler radar. *Monthly Weather Review*, *106*(1), 29–38. https://doi.org/10.1175/1520-0493(1978)106<0029:TDBPDR>2.0.CO;2

CalFire report (2018). CalFire Green Sheet: Burn Over Fatalities July 26, 2018, Carr Incident 18-CA-SHU-007808, 18-CA-SHU-007962, California Northern Region.

Church, C. R., Snow, J. T., & Dessens, J. (1980). Intense atmospheric vortices associated with a 1000 MW fire. *Bulletin of the American Meteorological Society*, *61*(7), 682–694.

Clements, C. B., Lareau, N. P., Kingsmill, D. E., Bowers, C. L., Camacho, C. P., Bagley, R., & Davis, B. (2018). RaDFIRE—The rapid deployments to wildfires experiment: Observations from the fire zone. *Bulletin of the American Meteorological Society*, *2018*. https://doi.org/10.1175/BAMS-D-17-0230.1

Countryman, C. M. (1971). *Fire whirls... why, when, and where*. Berkeley, CA: Pacific Southwest Forest and Range Experiment Station, Forest Service. US Department of Agriculture.

Cunningham, P., & Reeder, M. J. (2009). Severe convective storms initiated by intense wildfires: Numerical simulations of pyro-convection and pyro-tornadogenesis. *Geophysical Research Letters*, *36*, L12812. https://doi.org/10.1029/2009GL039262

Davies, J. M. (2006). Tornadoes in environments with small helicity and/or high LCL heights. *Weather and Forecasting*, *21*(4), 579–594. https://doi.org/10.1175/WAF928.1

Doswell, C. A., & Burgess, D. W. (1993). Tornadoes and tornadic storms: A review of conceptual models. *Geophysical Monograph-American Geophysical Union*, *79*, 161–161.

Forthofer, J. M., & Goodrick, S. L. (2011). Review of vortices in wildland fire. *Journal of Combustion*, *2011*, 1–14. https://doi.org/10.1155/2011/984363

Freitas, S. R., Longo, K. M., Chatfield, R., Latham, D., Silva Dias, M. A. F., Andreae, M. O., et al. (2007). Including the sub-grid scale plume rise of vegetation fires in low resolution atmospheric transport models. *Atmospheric Chemistry and Physics*, *7*(13), 3385–3398. https://doi.org/10.5194/acp-7-3385-2007

Fromm, M., Lindsey, D. T., Servranckx, R., Yue, G., Trickl, T., Sica, R., Doucet, P., et al. (2010). The untold story of pyrocumulonimbus. *Bulletin of the American Meteorological Society*, *91*(9), 1193–1210. https://doi.org/10.1175/2010BAMS3004.1

Fromm, M., Tupper, A., Rosenfeld, D., Servranckx, R., & McRae, R. (2006). Violent pyro-convective storm devastates Australia's capital and pollutes the stratosphere. *Geophysical Research Letters*, *33*, L05815. https://doi.org/10.1029/2005GL025161

Horel, J., Splitt, M., Dunn, L., Pechmann, J., White, B., Ciliberti, C., et al. (2002). Mesowest: Cooperative mesonets in the western United States. *Bulletin of the American Meteorological Society*, *83*(2), 211–225. https://doi.org/10.1175/1520-0477(2002)083<0211:MCMITW>2.3.CO;2

Jones, T. A., & Christopher, S. A. (2010). Satellite and radar remote sensing of southern Plains grass fires: A case study. *Journal of Applied Meteorology and Climatology*, *49*(10), 2133–2146. https://doi.org/10.1175/2010JAMC2472.1

Kuwana, K., Sekimoto, K., Minami, T., Tashiro, T., & Saito, K. (2013). Scale-model experiments of moving fire whirl over a line fire. *Proceedings of the Combustion Institute*, *34*(2), 2625–2631. https://doi.org/10.1016/j.proci.2012.06.092

Lakshmanan, V., Hondl, K., Potvin, C. K., & Preignitz, D. (2013). An improved method for estimating radar echo-top height. *Weather and Forecasting*, *28*(2), 481–488. https://doi.org/10.1175/WAF-D-12-00084.1

Lareau, N. P., & Clements, C. B. (2016). Environmental controls on pyrocumulus and pyrocumulonimbus initiation and development. *Atmospheric Chemistry and Physics*, *16*(6), 4005–4022. https://doi.org/10.5194/acp-16-4005-2016

Lee, B. D., & Wilhelmson, R. B. (1997). The numerical simulation of non-supercell tornadogenesis. Part I: Initiation and evolution of pretornadic misocyclone circulations along a dry outflow boundary. *Journal of the Atmospheric Sciences*, *54*(1), 32–60. https://doi.org/10.1175/1520-0469(1997)054<0032:TNSONS>2.0.CO;2

Luderer, G., Trentmann, J., & Andreae, M. O. (2009). A new look at the role of fire-released moisture on the dynamics of atmospheric pyro-convection. *International Journal of Wildland Fire*, *18*(5), 554–562. https://doi.org/10.1071/WF07035

Luderer, G., Trentmann, J., Winterrath, T., Textor, C., Herzog, M., Graf, H. F., & Andreae, M. O. (2006). Modeling of biomass smoke injection into the lower stratosphere by a large forest fire (Part II): Sensitivity studies. *Atmospheric Chemistry and Physics*, *6*(12), 5261–5277. https://doi.org/10.5194/acp-6-5261-2006

McCarthy, N., McGowan, H., Guyot, A., & Dowdy, A. (2017). Mobile X-Pol radar: A new tool for linvestigating pyroconvection and associated wildfire meteorology. *Bulletin of the American Meteorological Society*. https://doi.org/10.1175/BAMS-D-16-0118.1

McRae, R. H., Sharples, J. J., Wilkes, S. R., & Walker, A. (2013). An Australian pyro-tornadogenesis event. *Natural Hazards*, *65*(3), 1801–1811. https://doi.org/10.1007/s11069-012-0443-7

Nauslar, N., Abatzoglou, J., & Marsh, P. (2018). The 2017 North Bay and Southern California fires: A case study. *Fire*, *1*(1), 18. https://doi.org/10.3390/fire1010018

Peterson, D. A., Fromm, M. D., Solbrig, J. E., Hyer, E. J., Surratt, M. L., & Campbell, J. R. (2017). Detection and inventory of intense pyroconvection in western North America using GOES-15 daytime infrared data. *Journal of Applied Meteorology and Climatology*, *56*(2), 471–493. https://doi.org/10.1175/JAMC-D-16-0226.1

Peterson, D. A., Hyer, E. J., Campbell, J. R., Solbrig, J. E., & Fromm, M. D. (2017). A conceptual model for development of intense pyrocumulonimbus in western North America. *Monthly Weather Review*, *145*(6), 2235–2255. https://doi.org/10.1175/MWR-D-16-0232.1

Potter, B. E. (2005). The role of released moisture in the atmospheric dynamics associated with wildland fires. *International Journal of Wildland Fire*, *14*, 77–84. https//doi.org/10.1071/WF04045

Seto, D., & Clements, C. B. (2011). Fire whirl evolution observed during a valley wind-sea breeze reversal. *Journal of Combustion*, *2011*, 1–12. https://doi.org/10.1155/2011/569475

Sharples, J. J., Kiss, A. E., Raposo, J., Viegas, D. X. and Simpson, C. C., 2015. Pyrogenic vorticity from windward and lee slope fires. *Int. Congr. Model. Simul., Gold Coast, Aust. 29 Nov.–4 Dec*. (pp. 291–97).

Smith, B. T., Thompson, R. L., Dean, A. R., & Marsh, P. T. (2015). Diagnosing the conditional probability of tornado damage rating using environmental and radar attributes. *Weather and Forecasting*, *30*(4), 914–932. https://doi.org/10.1175/WAF-D-14-00122.1

Tohidi, A., Gollner, M. J., & Xiao, H. (2018). Fire whirls. *Annual Review of Fluid Mechanics*, *50*(1), 187–213. https://doi.org/10.1146/annurev-fluid-122316-045209

Tory, K. J., Thurston, W., & Kepert, J. D. (2018). Thermodynamics of pyrocumulus: A conceptual study. *Monthly Weather Review*, *146*(8), 2579–2598. https://doi.org/10.1175/MWR-D-17-0377.1

Trapp, R. J., Mitchell, E. D., Tipton, G. A., Effertz, D. W., Watson, A. I., Andra, D. L., & Magsig, M. A. (1999). Descending and nondescending tornadic vortex signatures detected by WSR-88Ds. *Weather and Forecasting*, *14*(5), 625–639. https://doi.org/10.1175/1520-0434(1999)014<0625:DANTVS>2.0.CO;2

Trentmann, J., Luderer, G., Winterrath, T., Fromm, M. D., Servranckx, R., Textor, C., et al. (2006). Modeling of biomass smoke injection into the lower stratosphere by a large forest fire (part I): Reference simulation. *Atmospheric Chemistry and Physics*, *6*(12), 5247–5260. https://doi.org/10.5194/acp-6-5247-2006

Umscheid, M. E., Monteverdi, J. P., & Davies, J. M. (2006). Photographs and analysis of an unusually large and long-lived firewhirl. *E-Journal of Severe Storms Meteorology*, *1*(2).

Wakimoto, R. M., & Wilson, J. W. (1989). Non-supercell tornadoes. *Monthly Weather Review*, *117*(6), 1113–1140. https://doi.org/10.1175/1520-0493(1989)117<1113:NST>2.0.CO;2

Zhou, R., & Wu, Z. N. (2007). Fire whirls due to surrounding flame sources and the influence of the rotation speed on the flame height. *Journal of Fluid Mechanics*, *583*, 313–345. https://doi.org/10.1017/S0022112007006337

Erratum

In the originally published version of this article, there were errors in the legend of Figure S1 in the main Supporting Information file. These errors have since been corrected, and the present version may be considered the authoritative version of record.